Progress In Electromagnetics Research M, Vol. 65, 29–42, 2018

Time-Domain Travelling-Wave Model for Quantum Dot Based Vertical Cavity Laser Devices

Ahmed E. Abouelez[1, *], Essam El Diwany[1], Mohamed B. El Mashade[2], and Hussein A. Konber[2]

Abstract—A self-consistent time-domain travelling-wave model for the simulation of self-assembled quantum dot (QD) vertical cavity surface emitting lasers (VCSELs) is developed. The 1-D time-domain travelling-wave model takes into consideration of time-varying QD optical susceptibility, refractive index variation resulting from intersubband free-carrier absorption, homogeneous and inhomogeneous broadening, and QD spontaneous emission noise source. Carrier concentration rate equations are considered simultaneously with the travelling wave model. Effects of temperature on optical susceptibility and carrier density in the active region are taken into account. The model is used to analyze the characteristics of 1.3-μm oxide-confined QD InAs-GaAs VCSEL. The field distribution resulting from time-domain travelling-wave equations, in both the active region and distributed Bragg reflectors, is obtained and used in finding the device characteristics including light-current static characteristics considering the thermal effect. Furthermore, the dynamic characteristics and modulation frequency response are obtained in terms of inhomogeneous broadening.

1. INTRODUCTION

Vertical cavity surface emitting lasers (VCSELs) are very important light sources due to their promising applications in many areas, such as optical interconnects, free-space optical communications, and optical data storage [1]. VCSELs have several advantages compared with conventional edge-emitting lasers [2]. These advantages are due to low threshold current, circular and low divergence, non-astigmatic circular output beams, single longitudinal mode operation, testability at the wafer level and suitability for two-dimensional array integration.

Lasers with quantum dots (QDs) as gain media were predicted to offer significant improvements in lasing characteristics over lasers of higher dimensionality such as bulk, quantum well and quantum wire lasers. Such improvements are in terms of low threshold current, temperature-insensitive operation, wide modulation bandwidth, and high differential gain. These improvements are a result of the atomic-like nature of QDs due to the three-dimensional quantum confinement of carriers in QDs active region [3]. Materials in the form of QDs cover wide range of wavelengths such as ZnO/MgZnO QD nanostructure at 0.375-μm wavelength [4] and InAs/GaAs QD nanostructure at 1.3-μm wavelength [5].

Recently, the inherent compatibility of InAs/GaAs-based QD active regions to a high-contrast AlGaAs-GaAs distributed Bragg reflector (DBR) mirror presents an excellent solution for constructing VCSELs [6]. Moreover, arsenide technology is relatively cheap and easy to manufacture, and offers manageable ways to create efficient radial electrical and optical confinements with AlO native-oxide apertures as well as much better DBR arsenide mirrors [7]. VCSEL at 1.3-μm is considered as one of

Received 21 November 2017, Accepted 14 February 2018, Scheduled 24 February 2018

* Corresponding author: Ahmed E. Abouelez (a.e.abouelez@gmail.com).

[1] Microwave Engineering Department, Electronics Research Institute, Cairo, Egypt. [2] Electrical Engineering Department, Faculty of Engineering, Al-AZHAR University, Cairo, Egypt.

the high performance light sources for fiber optical communication systems in the original band (i.e., O-band 1.26–1.36 μm).

Until now, several static and dynamic characteristics of 1.3-μm InAs-GaAs QD VCSELs have been investigated experimentally [6–8]. Many theoretical models have been presented, such as as simple phenomenological rate equations model [9, 10]. In [11], finite-difference time-domain (FDTD) method is used together with QD Maxwell-Bloch equations to find electric field propagation and microscopic carrier dynamics. A complex model is presented in [12] to simulate room temperature threshold operation of GaAs-based QD VCSEL where the effective frequency method is used for optical modeling, and 3D finite-element method is used for both electrical and thermal modelings. A time-domain travelling-wave (TDTW) model is developed in [13] to describe the dynamic behavior of quantum-well (QW) based VCSEL. Also, TDTW models are developed to simulate edge-emitting QD-based laser devices [14, 15].

The goal of this manuscript is to present TDTW model for the simulation of static and dynamic characteristics of self-assembled 1.3-μm InAs-GaAs QD-VCSEL. To the best of our knowledge, this model has not been previously used in the analysis of the QD-VCSEL devices.

The field distribution in VCSEL is obtained and used in the analysis, together wit carrier concentration rate equations, taking into consideration of thermal effect using a simple temperature model. In this model, the detailed structure of Bragg reflectors and the active region and lateral optical field profile are considered. Time-varying QD optical susceptibility, refractive index variation resulting from the intersubband free-carrier absorption, homogeneous and inhomogeneous broadening are taken into consideration.

The paper is organized as follows. In Section 2, the device under investigation is described. In Section 3, the theoretical model is described, which includes the basic formulas of material susceptibility considering homogeneous and inhomogeneous broadening. The refractive index variation resulting from intersubband free-carrier absorption is considered. The one-dimensional travelling wave model is developed, and the wave propagation through the Bragg mirrors is described considering phase delay in layers. Exciton multi-population rate equations for carrier dynamics are described and linked to the travelling wave model. Temperature effects on the static performance are included. In Section 4, static and dynamic characteristics of the QD-VCSEL under consideration are explored. Finally, the conclusion is presented in Section 5.

2. VCSEL STRUCTURE

The investigated device is a nominal oxide-confined 1.3-μm InAs/GaAs QD-VCSEL which is similar, but not identical, to that reported in [7]. The VCSEL device is a 2-λ cavity inserted between two DBR mirrors as shown in Fig. 1. The active region in the cavity consists of nine layers, each of 5-nm thick $In_{0.15}Ga_{0.85}As$ QWs, and each QW layer contains one sheet of InAs dots with a surface density of $5 \times 10^{14}\,m^{-2}$ and inserted in barrier GaAs material. These nine layers are arranged in periodic gain structure (PGS) where the layers are distributed in the cavity in 3 stacks, with each stack containing 3 layers of InAs-InGaAs separated by 33 nm GaAs barrier. Each stack is placed around antinodes of the cavity standing wave to increase the light-matter interaction and to obtain high optical gain. The two DBRs surrounding the cavity consist of repeating pairs of quarter-wavelength thick, low and high refractive index layers. The bottom n-DBR and top p-DBR are composed of 33.5 and 24 pairs of ($Al_{0.9}Ga_{0.1}As$/GaAs), respectively. $Al_{0.9}Ga_{0.1}As$ has a lower refractive index, while GaAs has a higher refractive index. Both DBRs are graded with interface grading by linearly changing the Al mole fraction [7]. The graded interface has two major effects: reducing the device electrical resistance and reducing the effective reflection of each DBR mirror. To take into consideration of these two effects of the graded interface in the DBRs in a manageable way, we reduce the number of pairs in each DBR by three pairs. The first layer of the top or bottom mirror as seen from the inner cavity has to have a lower refractive index (i.e., $Al_{0.98}Ga_{0.02}As$) than the cavity material (i.e., GaAs) to form antinodes at cavity edges, thus locate the standing wave antinodes at the stacks locations [7]. The first layer of the upper DBR seen from the inner cavity is manufactured from $Al_{0.98}Ga_{0.02}As$, which is used to create 20-nm AlO_3 native oxide aperture of diameter equal to 12 μm. AlO_3 is assumed to have a refractive index of 1.5296. Due to the presence of the oxide layer, the field is confined radially, and the device has a step index-guided structure in the radial direction between the core, of the aperture diameter,

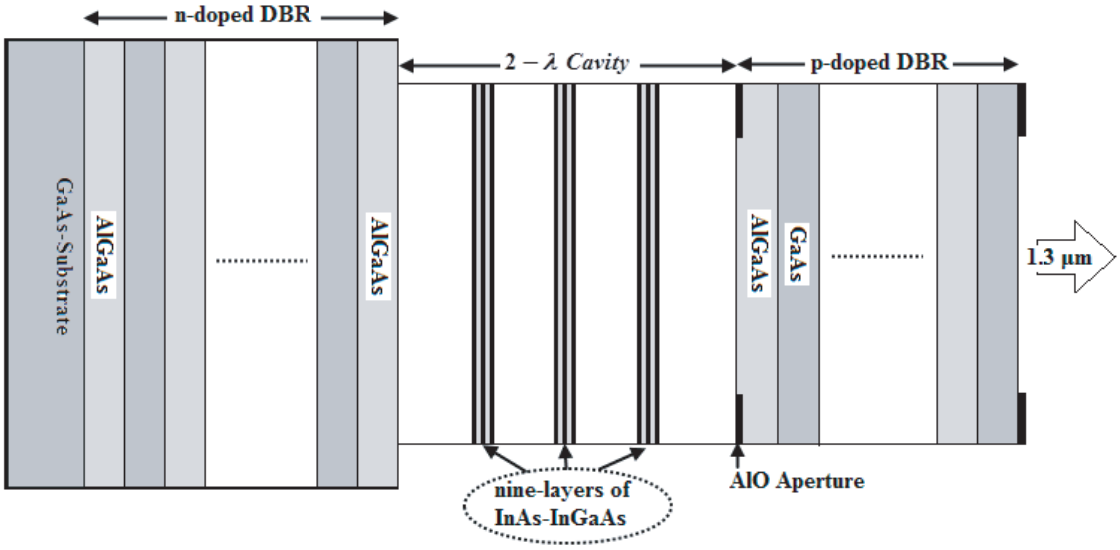

Figure 1. Schematic diagram of 1.3-μm QD VCSEL.

and the cladding [16]. Core refractive index is the refractive index of the layer material, while cladding refractive index is lower than that of the core because of the presence of the oxide layer with low refractive index. The core refractive indices of different materials are assumed to be 3.4109, 2.9514, 2.9185, 3.4504, and 3.4132 for GaAs, $Al_{0.9}Ga_{0.1}As$, $Al_{0.98}Ga_{0.02}As$, In(Ga)As (QW+QD) Layer, and Cavity (GaAs barrier & (QW+QD)), respectively [12]. The top mirror is terminated by air. It is of importance to note that this cavity has a Q-factor of approximately 7250 which is calculated according to [5]. This large Q-factor is due to the high reflectivity of DBRs (> 99.9). The QD-VCSEL device under consideration has a stopband of ~ 119.35 nm at 1.3 μm. This stopband is much wider than the range of variation of the wavelength due to temperature change. Finally, the absorption loss coefficient in each layer of the device is assumed as follows [12]: $1.6457\,\mathrm{cm}^{-1}$, $1.1861\,\mathrm{cm}^{-1}$ for (n-$Al_{0.9}Ga_{0.1}As$/n-GaAs), respectively. $0.85\,\mathrm{cm}^{-1}$, $3.0428\,\mathrm{cm}^{-1}$ for (p-$Al_{0.9}Ga_{0.1}As$/p-GaAs), respectively. For i-GaAs barrier, the loss is assumed to be $45\,\mathrm{cm}^{-1}$. Here we assume that the top mirror is terminated by air which is a low-index material. Diameters of the bottom and upper DBRs are equal to 250 μm and 22 μm, respectively, whereas the inner diameter of the p-contact region is assumed to be 12 μm.

3. THEORETICAL MODEL

The present theoretical model considers the dynamic buildup of the laser field due to the excitation current and presence of the spontaneous noise of the active material. The problem considers the interaction of the carrier density in the active material with the electric field. The carrier density introduces material susceptibility which affects the buildup of the electric field. The electric field, with its corresponding photon density, contributes, in turn, to carrier density rate equations. The following sections give the details of this model.

3.1. Active Material Susceptibility Model

As described in the previous section, each layer in the active region is composed of InAs QD layers embedded in InGaAs QWs (dot-in-a-well) and emitting at around 1.3 μm. Energy bands in the device cavity are as follows. Confined states for carriers in the QDs are supposed to consist of a two-fold degenerate ground state (GS), first excited state ($ES1$) with degeneracy equal to 4, and second excited state ($ES2$) with degeneracy equal to 6, respectively [14]. At higher energies, a continuum of 2-D states belonging to the QW and 3-D states in the GaAs barrier are considered. The transition energy for the GS is assumed to be 0.9616 eV, which corresponds to 1.3-μm radiation. The energy separation between

two successive confined states in conduction band are 61.1, 46.3, 36.9, and 88.1 meV for ΔE_{ES1-GS}, $\Delta E_{ES2-ES1}$, ΔE_{W-ES2}, and ΔE_{B-W}, respectively [14]. Furthermore, we consider that the electron-hole pair is localized in a dot as an indivisible exciton. In the exciton model, the occupancy of the hole energy level is the same as that of the corresponding electron level.

Due to the self-assembling growth process, QDs exhibit size and composition fluctuations, producing an inhomogeneous broadening for the density of states of the whole QD system [17]. In order to obtain the susceptibility of the QDs with corresponding different resonant energies, the whole QD ensemble is subdivided into $n = (2N + 1)$ discrete groups separated by energy difference of ΔE. The resonant energies for ith QD confined state (GS, $ES1$, and $ES2$) of the nth QD group are given by $E_{n,i} = E_i - ((N + 1) - n)\Delta E$, where E_i is the interband resonant energy of the central group. The inhomogeneous broadening due to fluctuation in QD size distribution is usually described by Gaussian distribution $G(E_{n,GS})$ around the center energy E_{GS} for the ground state, which holds also for any confined state E_i, as follows [17];

$$G\left(E_{n,GS}\right) = \frac{1}{\sqrt{2\pi}\sigma_o} \exp\left(-\frac{\left(E_{n,GS} - E_{GS}\right)^2}{2\sigma_o^2}\right) \tag{1}$$

where full-width at half maximum (FWHM) of the inhomogeneous broadening is $F_{inh} = 2.35\sigma_o$ for all confined states. $E_{n,GS}$ is the transition energy for each group for GS. The existence probability of the nth QD group is approximately given by $G_n = G(E_{n,GS})\Delta E$ and $\sum_n G_n = 1$.

The linear optical susceptibility $\chi_{GS,n}(r, t, \omega_m)$ of QD ground state active material is considered with the above mentioned inhomogeneous broadening and with homogeneous broadening $L(\omega_m)$. Furthermore, its dependence on the electron dynamics $\rho_{n,GS}(rt)$ is considered as a function of the radius r since the mode field distribution is a function of the radius. The linear optical susceptibility of QD at an angular frequency of the mth cavity mode ω_m is given by [14, 17];

$$\chi_{n,GS}\left(r,t,\omega_m\right) = jC_{n,GS} \times \left(2\rho_{n,GS}\left(r,t\right) - 1\right) L\left(\omega_m\right) \tag{2a}$$

$$C_{n,GS} = D_{GS} N_{3D} G_n \left(\frac{q^2 \pi \left|P_{GS}^{\sigma}\right|^2}{\varepsilon_o m_o^2 \omega_m}\right) \frac{1}{\pi \hbar \Gamma_{cv}} \tag{2b}$$

$$\rho_{n,i} = \frac{N_{n,i}}{D_i N_{3D} G_n}, \quad i = GS \tag{2c}$$

$$L\left(\omega_m\right) = \frac{\Gamma_{cv}}{\Gamma_{cv} + j\left(\omega_m - \omega_{n,GS}\right)} \tag{2d}$$

where, $C_{n,GS}$ is a constant factor; $\rho_{n,i}$ is the occupation probability of nth QDs group and ith energy level; $N_{n,i}$ is the carrier density in the ith QD confined state of the nth QD group; D_i is a degeneracy of ith QD energy level. The carrier density will be obtained by the solution of the rate equations as will be described in the electrical model. $L(\omega_m)$ given by Eq. (2d) is a complex Lorentzian function in the frequency domain which describes the homogeneous broadening. In Eqs. (2a)–(2d), given that the VCSEL cavity supports only one optical resonant frequency ($m = 1$), all dot groups contribute to only a single mode which is assumed to be Bragg mirror resonant angular frequency ω_o equal to angular frequency ω_{GS} corresponding to transition energy for the GS. $\omega_{n,GS}$ is the angular frequency corresponding to transition energy of the nth QD group of GS. In Eq. (2b), $(N_{3D}G_n)$ gives QD volume density in the nth QD group, where $N_{3D} = N_{sd}/h_{QD}$ is the QD volume density, N_{sd} the QD surface density per layer, and h_{QD} the average QD height. Along with this, q, ε_o, and m_o are the electron charge, permittivity of free space, and free electron mass, respectively. $|P_{GS}^{\sigma}|^2$ is the momentum matrix element [17]. Momentum matrix element $|P_{GS}^{\sigma}|^2$ is calculated to be equal to 2.9848×10^{-30} kg eV. In Eq. (2d), the FWHM of the homogeneous broadening is $F_{hom} = 2\hbar\Gamma_{cv}$, and the value of $1/\Gamma_{cv}$ represents the characteristic dephasing time of the interband transition. The dephasing rate or scattering rate Γ_{cv} can be expressed as a function of temperature as described in [10, 18]. Dephasing rate is expressed as $\Gamma_{cv} = 1/\tau_c$, where τ_c is the average time between collisions which can be expressed as $\tau_c = (\tau_{ee}\tau_{hh})/(\tau_{ee}+\tau_{hh})$ [17], where the mean hole-hole scattering time is $\tau_{hh} = m_e^*\mu_n/q$, and mean electron-electron scattering time is $\tau_{ee} = m_h^*\mu_p/q$. m_e^* and m_h^* are the electron and hole effective masses of GaAs, respectively. The electron and hole carrier mobility of GaAs ($\mathrm{cm}^2/\mathrm{V{\cdot}s}$) is expressed

as $\mu_n = 7200(300/T(K))^{2.1}$ and $\mu_p = 380(300/T(K))^{2.1}$, respectively [19]. Now, the FWHM of the homogeneous broadening can be calculated as a function of temperature.

In addition to susceptibility, field equations are affected by refractive index variations which result from the intersubband free-carrier absorption (FCA), calculated according to the Drude formula as follow [20]

$$\Delta n_F(r,t,\omega_o) = -\frac{q^2}{2n_{eff}\varepsilon_o\omega_o^2}\left[\Gamma_z\left(\frac{N_W(r,t)}{m^*_{eW}}+\sum_{n,i}\frac{N_{n,i}(r,t)}{m^*_{eD}}\right)+\Gamma_B\frac{N_B(r,t)}{m^*_{eB}}\right] \tag{3}$$

where N_B and N_W are the carrier density in the barrier and QW, respectively. m^*_{eD}, m^*_{eW}, and m^*_{eB} are the electron effective masses of QD, QW, barrier materials, respectively. Electron effective mass of the GaAs barrier, $In_{0.15}Ga_{0.85}As$ QW, and InAs QD is $(0.0665)m_o$, $(0.06)m_o$, and $(0.023)m_o$ [21], respectively. $\Gamma_z = n_{l-stack}d_a/(2\Delta z)$, where $n_{l-stack}$ is the number of active layers per stack, d_a the active layer thickness, and $(2\Delta z)$ equal to a thickness of half wavelength in the device containing an active stack, while $\Gamma_B = 1-\Gamma_z$.

In the following subsection, the interaction between the electric field and QD susceptibility will be presented through the travelling wave model.

3.2. Travelling Wave Model

The electric field can be expressed in terms of a center frequency propagation multiplied by a slowly varying function. The electric field is expressed as a longitudinal profile $e(z,t)$ times the normalized fundamental transverse mode distribution $\psi_N(r;z)$ as follows [13, 22];

$$E(r,z,t) = \left[A^F(z,t)\exp(-j\beta_o z+j\omega_o t)+A^B(z,t)\exp(j\beta_o z+j\omega_o t)\right]\psi_N(r;z) = e(z,t)\,\psi_N(r;z) \tag{4}$$

$A^F(z,t)$ and $A^B(z,t)$ [V] are slowly varying envelopes of the forward and backward propagating waves, respectively. β_o is the corresponding mode propagation constant in a certain layer. The lateral distribution of the field is assumed to be the fundamental linearly polarized LP_{01} mode [23]. The intensity distribution of dimensionless lateral field $|\psi(r)|^2$ is then normalized by $2\pi\int_0^\infty|\psi(r)|^2rdr$ to get the normalized fundamental transverse mode distribution, $|\psi_N(r)|^2$ which has a dimension of $[1/m^2]$. The slowly varying envelope of the electric field can be shown to satisfy the following travelling wave equation in the longitudinal z direction for each of the forward and backward traveling waves [14, 15] as follows;

$$\begin{aligned}&\pm\frac{\partial A^{F/B}(z,t)}{\partial z}+\left(\frac{n_{eff}}{c}\right)\frac{\partial A^{F/B}(z,t)}{\partial t}\\ &= -\frac{\alpha_i}{2}A^{F/B}(z,t)-j\frac{\omega_o}{c}\Delta n_{F-eff}A^{F/B}(z,t)-\left(j\frac{1}{2}\frac{\omega_o}{cn_{eff}}\right)P^{F/B}_{eff}(z,t)+U^{F/B}_{sp}(t)\end{aligned} \tag{5}$$

In nonactive regions the last three terms do not contribute. n_{eff} is the effective refractive index of the mode, where the mode propagation constant $\beta_o = k_o n_{eff}$. The effective refractive index of the mode which can be calculated in terms of difference between the core and the cladding. Core refractive index is the refractive index of the layer material, while cladding refractive index is lower than that of the core because of the presence of the oxide layer with low refractive index. The effective difference between core and cladding refractive indices is calculated according to the method described in [16] which has a value of 0.0128. The fundamental mode effective refractive indices of the different materials are calculated to be 3.4100, 2.9503, 3.4495, and 3.4131 for GaAs, $Al_{0.9}Ga_{0.1}As$, In(Ga)As (QW+QD) Layer, and Cavity (i.e., GaAs barrier & (QW+QD)), respectively.

For any radially dependent parameter X, such as optical susceptibility or refractive index change due to the intersubband transitions, an effective value is used in the z-directional travelling wave equation, to be weighted by the lateral distribution of the field through the following relation $X_{eff} = \int_0^\infty X(r)|\psi_N(r)|^2rdr$ [13].

In Eq. (5), α_i is the absorption loss coefficient in each layer. Δn_{F-eff} is the effective value of refractive index change due to the free carriers. $U^{F/B}_{sp}(t)$ is the spontaneous emission field, to be

defined. The effective polarization $P^{F/B}(z,t)$ can be expressed as a summation over all QD groups for GS as $P^{F/B} = \Gamma_R \Gamma_Z \sum_n p_{n,GS}^{F/B}$ where Γ_R is the relative confinement factor for the device stacks, also called gain enhancement factor, which accounts for the effect of positioning the stacked gain layers at antinodes [24]. For the device under consideration $\Gamma_R \sim 1.73$, $p_{n,GS}^{F/B}$ can be calculated as a function of device radius as follows [14, 15];

$$p_{n,GS}^{F/B} = jC_{n,GS}\left(2\rho_{n,GS}\left(r,t\right)-1\right) I_n^{F/B}\left(z,t\right) \tag{6a}$$

$I_n^{F/B}(z,t)$ is a convolution integral between the complex Lorentzian function in the time domain and (forward/backward) slowly varying field amplitude, which represents time domain filtering of the field by the Lorentzian function. This convolution can be calculated by [14]

$$\begin{aligned} I_n^{F/B}\left(z,t\right) &= e^{j\left(\omega_{GS,n}-\omega_o\right)\Delta t} e^{-\Gamma_{cv}\Delta t} I_n^{F/B}\left(z,t-\Delta t\right) \\ &\quad + \frac{\Gamma_{cv}\Delta t}{2}\left[A^{F/B}\left(z,t\right) + A^{F/B}\left(z,t\right) e^{j\left(\omega_{GS,n}-\omega_o\right)\Delta t} e^{-\Gamma_{cv}\Delta t}\right] \end{aligned} \tag{6b}$$

Finally, to take into account the spontaneous emission field in the TW equation, an extra term $U_{sp}^{F/B}(t)$ is included in Eq. (5). The field buildup in the device is started by the spontaneous field $U_{sp}^{F/B}(t)$ which is obtained from random processes, $x_{r,n} = x_{1,n} + jx_{2,n}$ for the ground state groups. $x_{1,n}$ and $x_{2,n}$ for each n are independent and identically distributed Gaussian random process, which have zero mean and unity variance and completely uncorrelated in time. The forward and backward spontaneous field can be expressed as [22];

$$U_{sp}^{F/B} = \sum_n \sqrt{2\sqrt{\frac{\mu_o}{\varepsilon_o}}\frac{\beta_{sp}}{2}\frac{\Gamma_z \hbar\omega_o\left(c/n_{eff}\right) g_{sp-eff}^{peak}}{n_{eff}\Delta z^2}} I\left(x_{r,n},t\right) \tag{7a}$$

where μ_o is the magnetic permeability of vacuum, Δz the discretized layer thickness in the cavity, β_{sp} the spontaneous emission coupling factor [14], and g_{sp-eff}^{peak} the effective value of the peak spontaneous gain g_{sp}^{peak} corresponding to $\omega_m = \omega_{n,GS}$ in the Lorentzian function, where the peak spontaneous gain is given as a function of device radius by $g_{sp}^{peak} = (\omega_o/cn_{eff})C_{n,GS}(\rho_{Gs,n}(r,t))^2$. In Eq. (7a), $I(x_{r,n},t)$ represents the random process $x_{r,n}$ filtered by the time domain Lorentzian function and is given by [12]

$$\begin{aligned} I\left(x_{r,n},t\right) &= e^{j\left(\omega_{GS,n}-\omega_o\right)\Delta t} e^{-\Gamma_{cv}\Delta t} I\left(x_{r,n},t-\Delta t\right) \\ &\quad + \frac{\Gamma_{cv}\Delta t}{2}\left[x_{r,n}\left(t\right) + x_{r,n}\left(t-\Delta t\right) e^{j\left(\omega_{GS,n}-\omega_o\right)\Delta t} e^{-\Gamma_{cv}\Delta t}\right] \end{aligned} \tag{7b}$$

To take into account nonlinear gain suppression, the polarization term given by Eq. (6) and spontaneous gain g_{sp-eff}^{peak} are further multiplied by a factor of the form $1/(1+\varepsilon_c S(r,t))$, where ε_c [m^3] is the nonlinear gain coefficient, which is a function of FWHM of the homogeneous broadening and photon lifetime [17]. The nonlinear gain coefficient is calculated to be $8.7133 \times 10^{-23}\,\mathrm{m}^3$ at $T = 300\,\mathrm{K}$. $S(r,t)$ is the photon density inside the cavity, $S(r,t)$, which can be calculated simply from the energy density of the electric field through the following relation [25]

$$S\left(r,t\right) = \left(\frac{\varepsilon_o n_{eff}^2}{2\hbar\omega_o}\right)\left[\left|A^F\left(z,t\right)\right|^2 + \left|A^B\left(z,t\right)\right|^2\right]\left|\psi_N\left(r\right)\right|^2 \tag{8}$$

As will be described in the electrical model section, Eq. (8) can be considered as a link between the travelling waves amplitudes and stimulated emission term in rate equations.

3.3. Numerical Solution of the TDTW Equations and the Boundary Conditions

The distribution of $A^{F/B}(z,t)$ along the laser cavity and both bottom and top DBRs can be represented in the numerical implementation at $k+1$ interfaces at boundaries of dielectric layers, where k is the

total number of dielectric layers. The thickness of the ith dielectric layer is assumed equal to Δz_i, where i is an integer, and the position of the boundary between the ith and $(i-1)$th layers is z_i. Dielectric layer thickness Δz_i is varied according to its effective refractive index such that optical length is equal to a quarter wavelength ($\lambda_o/4/n_{eff}(i)$) which is a necessary condition for the operation of the DBR. A suitable choice for the relation between time and spatial steps in the z direction in the solution of Eq. (5) is ($\Delta t = \Delta z_i n_{eff}(i)/c$), Δt will be a constant time step. In the simulation, the traveling waves, $A^{F/B}(z,t)$, are advanced from one dielectric interface at time t to the next interface at $t+\Delta t$. Across active layers, where the QD stacks are placed, Eq. (5) can be solved with the first-order finite difference approximation, as follows [14];

$$\begin{aligned} & A^F(z_i+\Delta z_i, t+\Delta t) \\ = \; & A^F(z_i,t) + \left(-\frac{\alpha_i}{2} - jk_o\Delta n_{F-eff}(t)\right) A^F(z_i,t)\,\Delta z_i - jP^F_{eff}(z_i,t)\,\Delta z_i + U^F_{sp}(t)\,\Delta z_i \quad (9a) \\ & A^B(z_i, t+\Delta t) \\ = \; & A^B(z_{i+1},t) + \left(-\frac{\alpha_i}{2} - jk_o\Delta n_{F-eff}(t)\right) A^B(z_{i+1},t)\,\Delta z_i - jP^B_{eff}(z_{i+1},t)\,\Delta z_i + U^B_{sp}(t)\,\Delta z_i \quad (9b) \end{aligned}$$

At the interfaces between two layers, boundary conditions are applied. At each time step, the boundary conditions for reflection and transmission are applied to the propagating fields at the dielectric interfaces by using Eq. (10). The amplitudes of propagated fields in terms of incident fields at the boundary between the dielectric layers can be determined from the transfer matrix for normally incident plane wave as follows [24];

$$\begin{bmatrix} A^F_{out} \\ A^B_{out} \end{bmatrix} = \begin{bmatrix} t_{11} & r_{12} \\ r_{21} & t_{22} \end{bmatrix} \begin{bmatrix} A^F_{in}e^{-i\varphi} \\ A^B_{in}e^{-i\varphi} \end{bmatrix} \quad (10)$$

where the corresponding transmission coefficients are t_{11}=$2n_{eff}(i-1)/(n_{eff}(i)+n_{eff}(i-1))$, t_{22}=$2n_{eff}(i)/(n_{eff}(i)+n_{eff}(i-1))$ and the corresponding reflection coefficients are $r_{12}=-r_{21}=(n_{eff}(i)-n_{eff}(i-1))/(n_{eff}(i)+n_{eff}(i-1))$. As stated in the previous section, $A^F(z,t)$ and $A^B(z,t)$ are slowly varied with both z and t; however, the operation of the DBR requires that the length of each of its layers must be a quarter wavelength. Thus, a phase shift of $\varphi=(\pi/2)$ across the layer is included in Eq. (10). Thus the amplitudes (i.e., $A^F(z,t)$ and $A^B(z,t)$) should be slowly varied with respect to time, whereas they should include the phase variation with z as described. $n_{eff}(i)$ and $n_{eff}(i-1)$ are effective refractive indices of the mode in adjacent ith and $(i-1)$th layers, respectively. The boundary conditions at top and bottom surfaces of the Bragg reflectors can be written as

$$A^B(t,z_{k+1}) = r_R A^F_{in}(t,z_{k+1}), \quad \text{and} \quad A^F(t,z_1) = r_L A^B_{in}(t,z_1) \quad (11)$$

where the semiconductor-air reflectivity $r_R=0.55$ and semiconductor-metal reflectivity $r_L=-0.974$. The output power is calculated according to the following equation [25, 26];

$$P_{out} \approx \frac{c}{n_{eff}}\hbar\omega_o\left(1-|r_R|^2\right)\left(\frac{\varepsilon_o n^2_{eff}}{2\hbar\omega_o}\right)\left|A^F_{in}(z_{k+1})\right|^2 \quad (12)$$

3.4. Electrical Model and Rate Equations of Carrier Density

In the previous section, the QD material optical susceptibility is linked to the travelling wave through polarization term. In this section, dependence of susceptibility on carrier dynamics will be presented. Carrier dynamics are controlled by different parameters such as injected current, relaxation and escaping times between energy bands, spontaneous and nonradiative recombination times, and rate of stimulated emission. The carrier dynamics will be linked with the travelling wave model through the stimulated term in carrier concentration rate equations. The dynamics of carrier density as a function of device radius are presented in a set of rate equations. The first rate equation is for the carrier density in the 3-D barrier state. The second rate equation describes the carrier density in the 2-D QW state. Finally, there are n rate equations for the (electron) carrier density in each QD confined state of each QD group.

The rate equations are as follows [14];

$$\frac{dN_B\,(r,t)}{dt} = \frac{J\,(r,t)}{qn_l d_a}+\frac{N_W}{\tau_{W-B}}-\left(\frac{1}{\tau_{B-W}}\,(1-\rho_W)+\frac{1}{\tau_r^B}\right)N_B \tag{13a}$$

$$\frac{dN_W\,(r,t)}{dt} = \frac{N_B}{\tau_{B-W}}\,(1-\rho_W)+\sum_n \frac{N_{n,ES2}}{\tau_{n,ES2-W}}-\frac{N_W}{\tau_{W-ES2}}\sum_n (1-\rho_{n.ES2})\,G_n-\frac{N_W}{\tau_{W-B}}-\frac{1}{\tau_r^W} \tag{13b}$$

$$\begin{aligned}\frac{dN_{n,ES2}\,(r,t)}{dt} = {} & \frac{N_W G_n\,(1-\rho_{n,ES2})}{\tau_{W-ES2}}+\frac{N_{n,ES1}}{\tau_{ES1-ES2}}\,(1-\rho_{n.ES2})-\frac{N_{n,ES2}}{\tau_{ES2-ES1}}\,(1-\rho_{n,ES1}) \\ & -\frac{N_{n,ES2}}{\tau_{ES2-W}}\,(1-\rho_W)-\frac{N_{n,ES2}\rho_{n,ES2}}{\tau_{Aug}^{ES2}}-\frac{N_{n,ES2}}{\tau_r^{ES2}}\end{aligned} \tag{13c}$$

$$\begin{aligned}\frac{dN_{n,ES1}\,(r,t)}{dt} = {} & \frac{N_{n,ES2}}{\tau_{ES2-ES1}}\,(1-\rho_{n,ES1})+\frac{N_{n,GS}}{\tau_{GS-ES1}}\,(1-\rho_{n,ES1})-\frac{N_{n,ES1}}{\tau_{ES1-GS}}\,(1-\rho_{n,GS}) \\ & -\frac{N_{n,ES1}}{\tau_{ES1-ES2}}\,(1-\rho_{n,ES2})-\frac{N_{n,ES1}\rho_{n,ES1}}{\tau_{Aug}^{ES1}}-\frac{N_{n,ES1}}{\tau_r^{ES1}}\end{aligned} \tag{13d}$$

$$\frac{dN_{n,GS}\,(r,t)}{dt} = \frac{N_{n,ES1}}{\tau_{ES1-GS}}\,(1-\rho_{n,GS})-\frac{N_{n,GS}}{\tau_{GS-ES1}}\,(1-\rho_{n,ES1})-\frac{N_{n,ES1}\rho_{n,ES1}}{\tau_{Aug}^{GS}}-\frac{N_{n,ES1}}{\tau_r^{GS}}-R_{stimulated,n} \tag{13e}$$

In Eq. (13a), N_B is the carrier density in the barrier. n_l and d_a are the number of QD layers and active layer thickness, respectively. The occupation probability in the QW in Eq. (13b) is $\rho_W{=}N_W/DOS_W$ [21], where N_W is the carrier density in the QW. The effective density of states per unit volume in the QW layer is given by $DOS_W{=}(m_W^* k_B T/\pi\hbar^2 h_W)$, where h_W denotes the width of the QW. The total current density $J(r,t)$ is expressed as a function of device radius, which is given by the following relation [13];

$$J\,(r,t) = \begin{cases} J_o & r{\leq}r_{oxide} \\ J_o \exp\left(-\dfrac{(r-r_{oxide})}{r_s}\right) & r{>}r_{oxide}\end{cases} \tag{14}$$

where r_{oxide} and r_s are oxide aperture radius and current spread coefficient, respectively. Current spread coefficient is assumed equal to 0.02 μm [13]. J_o is the normalization coefficient for injected current I_{in}, which can be expressed as $J_o = I_{in}/\pi r_{oxide}^2$. The total carrier transport time from the barrier layer to the QW may be expressed as [19] $\tau_{B-W} = \tau_r + \tau_c$ where τ_c is the carrier capture time of the QW which in general is about 0.3–0.5 ps for typical QW lasers. On the other hand, τ_r is the carrier transport time from the barrier layer to QW, which can be expressed as [19] $\tau_r = (L_s^2/2D)$ where L_s is the distance measured from QW to the edge of the doped Bragg mirror which is equal to 190 nm. The ambipolar diffusion coefficient $D = 2D_e D_h/(D_e{+}D_h)$. The diffusion coefficient for electrons D_e and holes D_h can be calculated from the Einstein relation as $D_{e/h} = (k_B T/q)\mu_{e/h}$, where T and k_B are the temperature in Kelvin and Boltzmann's constant, respectively. τ_{W-B} is the escape time from the QW to the barrier.

In Eq. (13b), τ_{W-ES2} is the average relaxation time from QW to ES2 while $\tau_{n,ES2-W}$ is escape times from $ES2$ to QW for each QD group. τ_r^B and τ_r^W are carrier recombination times in GaAs barrier and InGaAs QW, respectively. Their values are assumed to be 400 ps [27].

Finally, Eqs. (13c)–(13e) represent n rate equations for the carrier density in each QD confined state. The carrier density $N_{n,i}$ in the ith QD state of the nth QD group is related to the corresponding occupation probability via Eq. (2c). The carrier lifetimes in GS, $ES1$, and $ES2$ are denoted by τ_r^{GS}, τ_r^{ES1} and τ_r^{ES2}, respectively. The carrier lifetime for all QD states is assumed equal to 1 ns. The characteristic Auger recombination times, τ_{Aug}^i with $i = GS$, $ES1$, $ES2$ QD confined states, are assumed to have the values of 660, 270, and 110 ps, respectively [14].

It is assumed that relaxation and capture times between energy levels exist only between adjacent states. Carriers relaxation time from QW to ES2 is expressed as $\tau_{W-ES2} = 1/(A_c + C_c N_W)$ which is assumed identical for all groups [28]. The average intradot relaxation times from the QD ith to jth levels with subscripts i, $j = GS$, $ES1$, $ES2$ can be expressed, with the hypothesis that the final state is empty, as $\tau_{i-j}(i \neq j) = 1/(A_o + C_o N_W)$ [21, 28]. A_c and A_o are phonon-assisted relaxation rates,

while C_c and C_o are Auger relaxation rates. The values of A_c and C_c are assumed to be $1\times10^{12}\,\mathrm{s}^{-1}$ and $1\times10^{-14}\,\mathrm{m}^3\,\mathrm{s}^{-1}$, respectively. A_o and C_o are assumed to be $5\times10^{11}\ \mathrm{s}^{-1}$ and $3.5\times10^{-13}\,\mathrm{m}^3\,\mathrm{s}^{-1}$, respectively [28].

Furthermore, there is an exponential relationship between the relaxation rate and escape rate. Escape times can be obtained from relaxation times from the relations described in [14]. The stimulated rate term in Eq. (13e) is given by;

$$R_{stimulated,n} = \Gamma_R\left(\frac{c}{n_{eff}}\right)\left[\frac{\omega_o}{cn_{eff}}C_{n,GS}\left(2\rho_{n,GS}\left(r,t\right)-1\right)\frac{1}{1+\varepsilon_c S\left(r,t\right)}\right] \times\left(\frac{\varepsilon_o n_{eff}^2}{2\hbar\omega_o}\left[R\left(A^{F*}\left(z,t\right)I_n^F\left(z,t\right)\right)+R\left(A^{B*}\left(z,t\right)I_n^B\left(z,t\right)\right)\right]\left|\psi_N\left(r\right)\right|^2\right) \tag{15}$$

Eqs. (13a)–(13e) represent therefore the complete set of equations to be solved numerically to determine the carrier dynamics at each lateral radius of the cavity under current injection. In the numerical solution, the carriers distributions N_B, N_W and $N_{n,i}$ along the lateral direction of the active region are calculated at l positions, $r_1 = 0$ to $r_l = (l-l)\Delta r$, where Δr is the separation between two successive points in the r-direction. The multi-population rate equations described in Eqs. (13a)–(13e) are solved at each lateral element r_l with a first-order finite difference approximation, to obtain the lateral occupation probabilities values in the QDs. The travelling wave amplitudes are linked to the rate equations through the stimulated rate term given by Eq. (15) where at each time step, the rate equations are solved simultaneously together with the TDTW equations. In the following subsection, the model will be completed with the description of the thermal effect.

3.5. Thermal Effect

Several parameters described in previous sections depend on temperature such as homogeneous broadening and escape times. In order for the model to be complete, the temperature effect must be included. The analysis of the temperature distribution for VCSEL requires complex numerical calculations [29]. Furthermore, the thermal process reaches its steady state in time in the order of microseconds [29]. This time is much longer than the carrier process steady state time which is in the order of nanoseconds. It is lengthy to simulate the static behavior of the VCSEL with the iterative technique described in [30] with our complex travelling wave model. In this work, we will follow a simple approach that considers the temperature rise ΔT by joule heating as a function of the injected current I_{in}, thermal resistance $R_{th}\,(\mathrm{K/W})$ and device series resistance $R_s\,(\Omega)$, where the temperature at steady state is given as [23];

$$T = T_o + \left(R_{th}R_sI_{in}^2\right) \tag{16a}$$

where T_o is the ambient temperature (i.e., $T_o = 300\,\mathrm{K}$). Series resistance R_s is a device parameter. The calculation of thermal resistance is based on an approximate analytical formula, derived in [31], which considers the thermal resistance corresponding to a uniform heat flow in the vertical direction through the cylinder of the device diameter D_s in addition to a term which approximates the spreading resistance of thermal contact. This equation has the following form

$$R_{th} \approx \frac{4d_{eff}}{\pi k_{eff}D_s^2} + \frac{1}{2k_{eff}D_{oxide}}\left(1-\frac{D_{oxide}}{D_s}\right)^{3/2} \tag{16b}$$

where $d_{eff} = k_{eff}\sum\limits_i(\Delta z_i/k_i)$ is the effective thickness of the n-DBR mirror and substrate, while $k_{eff} = \sum\limits_i \Delta z_i k_i / \sum\limits_i \Delta z_i$ is the effective thermal conductivity [24]. k_i and Δz_i are the thermal conductivity and thickness in the ith layer of n-DBR mirror, respectively. D_{oxide} and D_s are oxide aperture diameter and total device diameter. The second term in Eq. (16b) represents the spreading resistance of thermal contact. The parameters required for the calculation of thermal resistance are as follows: the thermal conductivity for n-GaAs is 44.05 $(\mathrm{Wm^{-1}\,K^{-1}})$ and for n-AlGaAs is 25.35 $(\mathrm{Wm^{-1}\,K^{-1}})$ [12]. Device series resistance R_s is assumed to be $1000\,(\Omega)$ [7]. Now, the temperature in the thermal steady state as a function of injected current can be calculated through Eqs. (16a)–(16b). Thus, this value is used in the

determination of static characteristics. For optical dynamic behavior, in the order of nanoseconds, the temperature rise is in the order of fraction or few degrees [29], thus it is reasonable to use the ambient temperature in simulating optical dynamic behavior.

4. SIMULATION RESULTS AND DISCUSSION

In this section, results of the investigated model will be presented. First, static results are of primary concern. It is assumed that the QDs are divided into 9 groups with FWHM of inhomogeneous broadening of 40 meV. Fig. 2(a) shows the temperature rise as a function of the applied current. This figure includes also the FWHM of the homogeneous broadening which corresponds to the temperature rise. This rise is proportional to the square of the input current as we have shown in Eq. (16a). The dephasing rate Γ_{cv} can be calculated as a function of this temperature rise, and this in turn can be used to evaluate the FWHM of the homogeneous broadening.

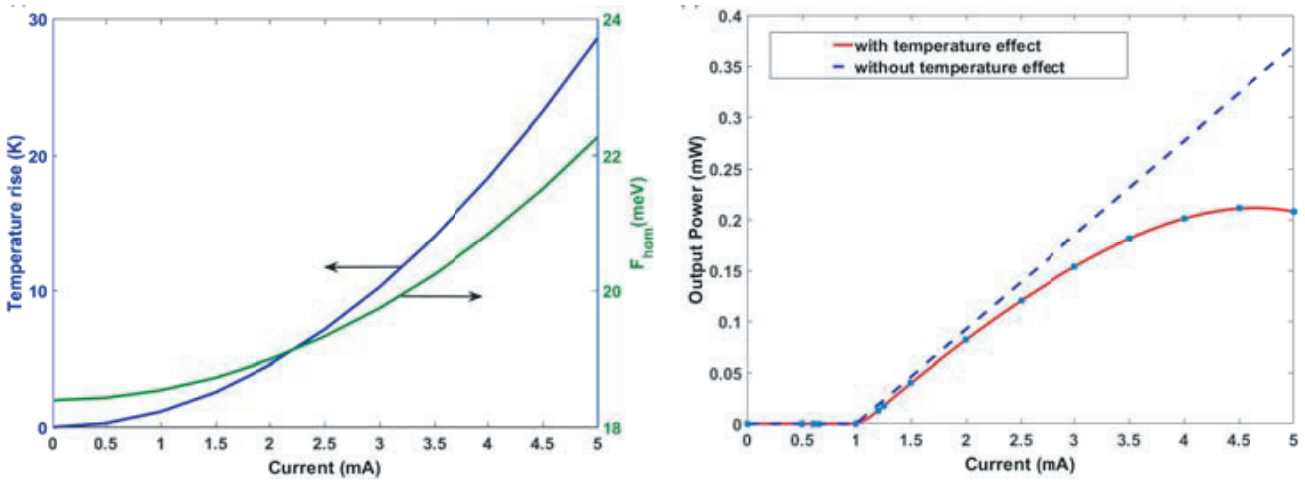

Figure 2. (a) The temperature rise (left scale), and FWHM of homogeneous broadening (right scale), in the active region as a function of the input current. (b) Output power as a function of the input current, with and without temperature effect.

Figure 2(b) illustrates the steady state output power as a function of the applied current with and without temperature rise effects. The output power is calculated according to Eq. (12). As expected, without taking into consideration of effects of temperature rise, the output power linearly increases from threshold current, $I_{th} \approx 1\,\text{mA}$, with an increase of the applied current. On the other hand, when temperature effects are taken into consideration, the output power curve is lower than that corresponding to output power curve without temperature effect. The rollover occurs at a current $\approx 4.5\,\text{mA}$ (i.e., $\approx 4.5 I_{th}$). These effects can be explained as follows; as the temperature increases, the dephasing rate increases, which will result in more reduction in gain as Eq. (2) indicates. Moreover, the temperature rise enhances the escaping rate of carriers that will result in a reduction in the population inversion term (i.e., $(2\rho - 1)$) which is considered as another reduction in gain. There are other effects of temperature rise which are not taken into consideration in this work, such as thermal lensing effect which means the effect of temperature rises on the refractive index. In addition, temperature rise affects the energy gap of cavity materials (i.e., GaAs, InGaAs, and InAs) which results in a red shift of the lasing wavelength. It is known that in semiconductor laser, the peak gain wavelength is temperature dependent; however, QD based semiconductor laser enjoys, theoretically, stable emission wavelength since its transition energy is nearly unaffected by the changes of the operating conditions [5, 17]. So, we have neglected temperature-wavelength dependence in this work.

In Figs. 3 and 4, we plot field distributions along the device, $z = 0$ which corresponds to the interfacing between the GaAs substrate and AlGaAs half pair (i.e., interface number one). The interface

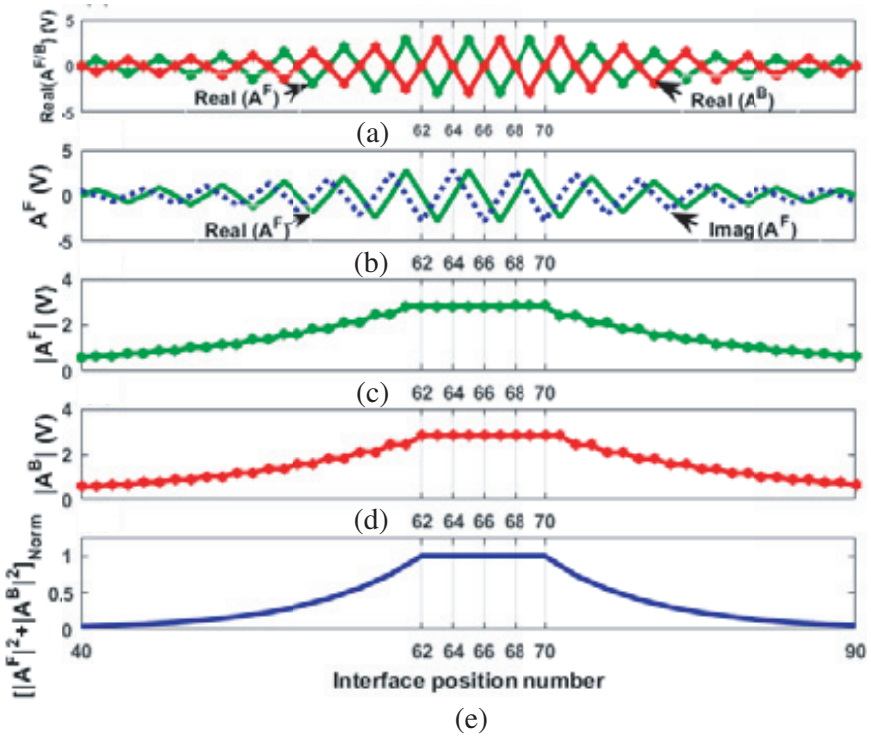

Figure 3. (a) Distribution of real part of forward and backward field amplitude as a function of the interface position number. (b) Distribution of real and imaginary parts of forward field amplitude as a function of the interface position number. (c) Slowly varying envelope of the forward field. (d) Slowly varying envelope for the backward field. (e) Normalized photon density distribution along the device.

between GaAs and air is the last interface. The cavity extends between interface numbers 62 and 70.

Figure 3(a) shows real parts of complex amplitudes A^F and A^B at steady state. At cavity edges, real parts of A^F and A^B are nearly equal representing nearly unity reflection coefficients from DBRs. Fig. 3(b) shows real and imaginary parts of A^F. Their peaks are shifted by $(\pi/2)$ and can, for example, be represented within the cavity by $-j\exp[-j(\pi/2)(i-62)]$ which can be viewed as including the z dependence of the forward travelling wave, where i is the interface position number. The backward wave can be expressed similarly. The standing wave intensity in Fig. 4(e) becomes thus $(\cos^2[(\pi/2)(i-62)])$. Figs. 3(c)–(d) show absolute values of A^F and A^B while Fig. 3(e) corresponds to the normalized local photon density along the vertical cavity structure. Generally, the patterns in Fig. 3 are nearly coincident at successive time steps according to their slow variation with time.

Second, dynamic results will be presented. Fig. 4(a) shows the effective refractive index distribution along the z direction. Figs. 4(b)–(e) show the intensity buildup at different times, from dominant spontaneous noise ((b), (c), and (d)) to steady state in (e), defined as I_{LP01}=$|A^F+A^B|^2$. As expected, standing wave antinodes are located at the positions of active QD stacks. Outside the cavity, in DBRs, the field attenuates away from the cavity.

Now, in order to examine the effect of FWHM of inhomogeneous broadening on the turn-on dynamics as well as the modulation frequency response, different values of the inhomogeneous broadening of 20, 30, and 40 meV are chosen for comparison. The turn-on dynamics and modulation response are studied at a constant applied current of 2 mA (i.e., $2I_{th}$). As shown in Fig. 5(a), the turn-on delay time increases with higher inhomogeneous broadening. It is defined as the time required to reach the laser threshold. Moreover, the higher inhomogeneous broadening results in lower steadystate output intensity and slower relaxation oscillations frequency which limits small-signal modulation response of the laser. The small-signal modulation response and modulation bandwidth are shown in Fig. 5(b). The response is obtained by applying a small change of current (small step) at steady state and finding

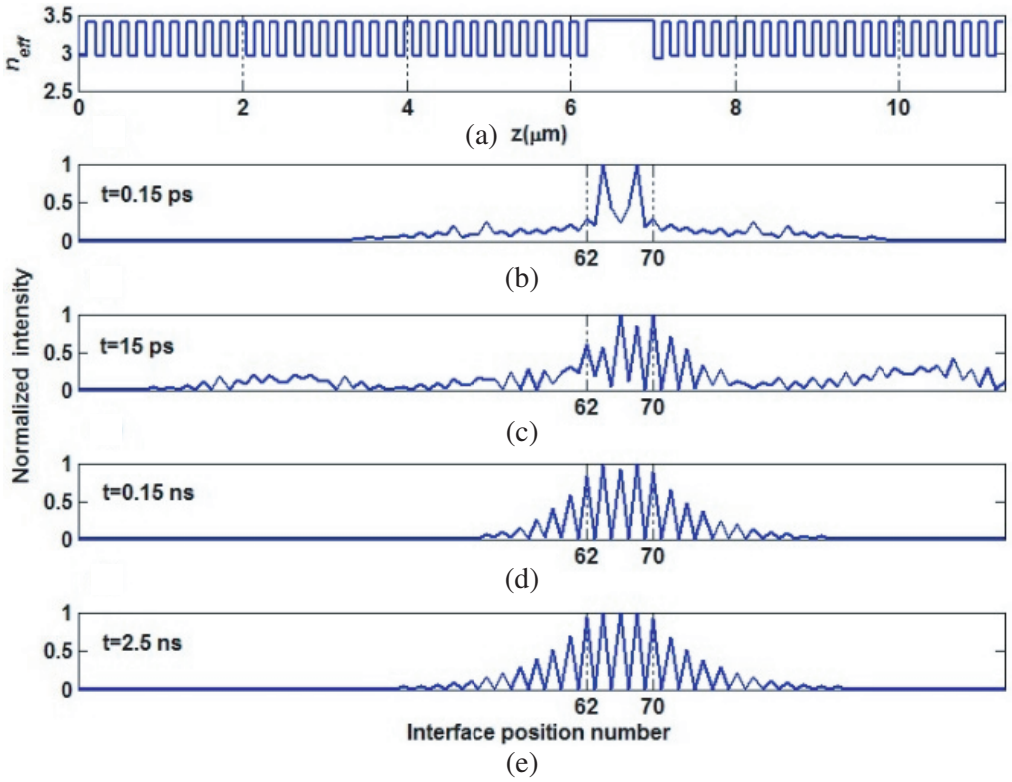

Figure 4. (a) Refractive index profile along the laser z-axis. (b)–(e) The intensity distribution of the standing wave, at different times, of the fundamental LP_{01} mode along the laser z-axis, expressed by the interface position number within VCSEL under consideration.

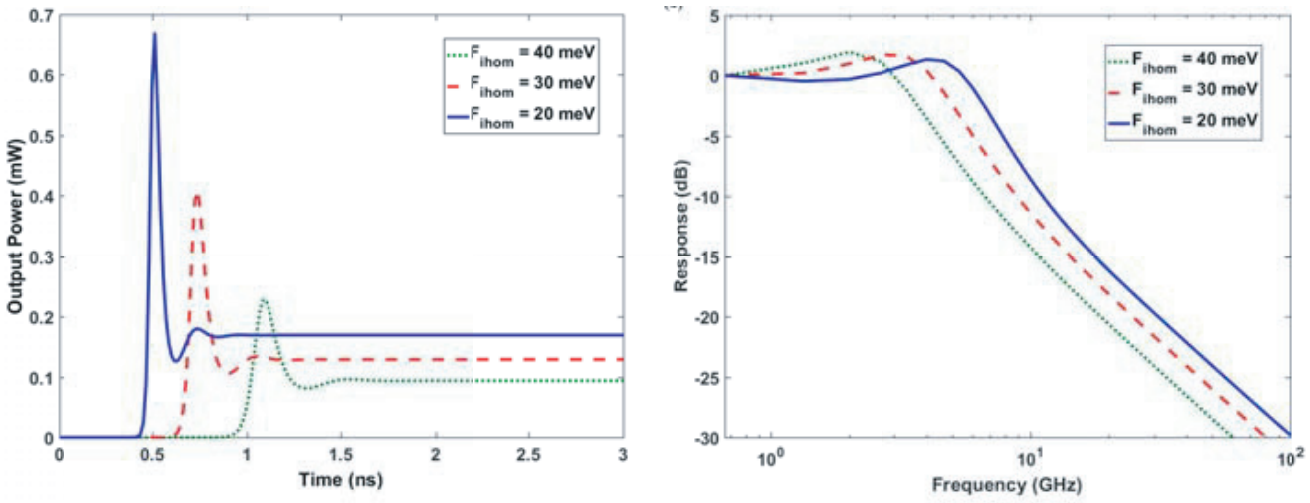

Figure 5. (a) Output power turn-on dynamics for different values of inhomogeneous broadening at an input current of 2 mA. (b) Frequency response for different values of the inhomogeneous broadening at an input current of 2 mA.

the Fourier transform of the transient emission. As expected, 3-dB modulation bandwidth decreases as the inhomogeneous broadening increases. Such a behavior shown in Figs. 5(a) and (b) results is due to the increase of the inhomogeneous broadening leading to lower modal gain and higher threshold current and therefore degrades the frequency response and also results in longer turn-on delay time.

5. CONCLUSIONS

A self-consistent time-domain travelling-wave model for the simulation of self-assembled QD-VCSELs is developed for considering the detailed field and carriers distributions in the VCSEL. Complete 1-D time-domain travelling-wave equations and carrier concentration rate equations are considered simultaneously. The effects of temperature are taken into account. The model is used to analyze the characteristics of 1.3-µm oxide-confined QD InAs-GaAs VCSEL. The field distribution resulting from time-domain travelling-wave equations, in both the active region and DBRs, is obtained and used in finding the device characteristics including light-current static characteristics considering the thermal effect. Furthermore, the dynamic characteristics and modulation frequency response are obtained showing the effect of inhomogeneous broadening.

REFERENCES

1. Larsson, A., "Advances in VCSELs for communication and sensing," *IEEE J. Sel. Topics Quantum Electron.*, Vol. 17, No. 6, 1552–1567, 2011.
2. Towe, E., R. F. Leheny, and A. Yang, "A historical perspective of the development of the vertical-cavity surface-emitting laser," *IEEE J. Sel. Topics Quantum Electron.*, Vol. 6, No. 6, 1458–1464, 2000.
3. Mukai, K., Y. Nakata, K. Otsubo, M. Sugawara, N. Yokoyama, and H. Ishikawa, "1.3 µm CW lasing characteristics of self-assembled InGaAs-GaAs quantum dots," *IEEE J. Quantum Electron.*, Vol. 36, 472–478, Apr. 2000.
4. Zope, U., E. P. Samuel, M. P. Bhole, and D. S. Patil, "Optical field distribution in ZnO/MgZnO quantum dot nanostructure at 375-nm wavelength," *Physica E*, Vol. 42, 38–42, 2009.
5. Ustinov, V. M., *Quantum Dot Lasers*, Oxford Univ. Press, Oxford, 2007.
6. Ding, Y., W. J. Fan, D. W. Xu, L. J. Zhao, Y. Liu, and N. H. Zhu, "Fabrication and characterization of 1.3-µm InAs quantum-dot VCSELs and monolithic VCSEL arrays," *Proc. SPIE-OSA-IEEE*, Vol. 7631, 763102-1–763102-7, 2010.
7. Yu, H. C., J. S. Wang, Y. K. Su, S. J. Chang, F. I. Lai, Y. H. Chang, H. C. Kuo, C. P. Sung, H. P. D. Yang, K. F. Lin, J. M. Wang, J. Y. Chi, R. S. Hsiao, and S. Mikhrin, "1.3 µm InAs-InGaAs quantum-dot vertical-cavity surface-emitting laser with fully doped DBRs grown by MBE," *IEEE Photonics Technology Letters*, Vol. 18, No. 2, 418–420, 2006.
8. Tong, C. Z., D. W. Xu, S. F. Yoon, Y. Ding, and W. J. Fan, "Temperature characteristics of 1.3-µm p-doped InAs-GaAs quantum-dot vertical cavity surface-emitting lasers," *IEEE J. Sel. Topics Quantum Electron.*, Vol. 15, No. 3, 743–748, 2009.
9. Xu, D. W., S. F. Yoon, and C. Z. Tong, "Self-consistent analysis of confinement and output power in 1.3 µm InAs-GaAs quantum-dot VCSELs," *IEEE J. Quantum Electron.*, Vol. 44, No. 9, 879–885, 2008.
10. Abbaspour, H., V. Ahmadi, and M. H. Yavari, "Analysis of QD VCSEL dynamic characteristics considering homogeneous and inhomogeneous broadening," *IEEE J. Sel. Topics Quantum Electron.*, Vol. 17, No. 5, 1327–1333, 2011.
11. Kim, J. E., E. Malić, M. Richter, A. Wilms, and A. Knorr, "Maxwell-Bloch equation approach for describing the microscopic dynamics of quantum-dot surface-emitting structures," *IEEE J. Quantum Electron.*, Vol. 46, No. 7, 1115–1126, 2010.
12. Piskorski, Ł., M. Wasiak, R. Sarzała, and W. Nakwaski, "Structure optimisation of modern GaAs-based InGaAs/GaAs quantum-dot VCSELs for optical fibre communication," *Opto-Electronics Review*, Vol. 17, No. 3, 217–224, 2009.
13. Yu, S. F., "Dynamic behavior of vertical-cavity surface-emitting lasers," *IEEE Journal of Quantum Electronics*, Vol. 32, No. 7, 1168–1179, 1996.
14. Rossetti, M., P. Bardella, and I. Montrosset, "Time-domain travelling-wave model for quantum dot passively mode-locked lasers," *IEEE Journal of Quantum Electronics*, Vol. 47, No. 2, 139–150, 2011.

15. Gioannini, M. and M. Rossetti, "Time-domain traveling wave model of quantum dot DFB lasers," *IEEE J. Sel. Topics Quantum Electron.*, Vol. 17, No. 5, 1318–1326, 2011.
16. Michalzik, R., "Simple understanding of waveguiding in oxidized VCSELs," *Annu. Rep. 1*, 19–23, Dept. Optoelectron., Univ. Ulm, Ulm, Germany, 1995.
17. Sugawara, M., *Self-assembled InGaAs/GaAs Quantum Dots: Semiconductors and Semimetals*, Vol. 60, Academic Press, San Diego, CA, 1999.
18. Banihashemi, M. and V. Ahmadi, "Dynamic characteristics of photonic crystal quantum dot lasers," *Applied Optics*, Vol. 53, No. 12, 2595, 2014.
19. Tansu, N. and L. J. Mawst, "Current injection efficiency of InGaAsN quantum-well lasers," *Journal of Applied Physics*, Vol. 97, No. 5, 054502, 2005.
20. Kim, J., C. Meuer, D. Bimberg, and G. Eisenstein, "Effect of inhomogeneous broadening on gain and phase recovery of quantum-dot semiconductor optical amplifiers," *IEEE Journal of Quantum Electronics*, Vol. 46, No. 11, 1670–1680, 2010.
21. Tong, C., S. Yoon, C. Ngo, C. Liu, and W. Loke, "Rate equations for 1.3-μm dots-under-a-well and dots-in-a-well self-assembled InAs-GaAs quantum-dot lasers," *IEEE Journal of Quantum Electronics*, Vol. 42, No. 11, 1175–1183, 2006.
22. Li, X., "Distributed feedback lasers: Quasi-3D static and dynamic model," *Optoelectronic Devices. Advanced Simulation and Analysis*, 87–119, J. Piprek (ed.), Springer, Berlin, 2005.
23. Mulet, J. and S. Balle, "Mode-locking dynamics in electrically driven vertical-external-cavity surface-emitting lasers," *IEEE Journal of Quantum Electronics*, Vol. 41, No. 9, 1148–1156, 2005.
24. Yu, S. F., *Analysis and Design of Vertical Cavity Surface Emitting Lasers*, John Wiley & Sons, 2003.
25. Agrawal, G. P. and N. K. Dutta, *Semiconductor Lasers*, 2nd Edition, Van Nostrand, New York, 1993.
26. Yu, S. F., "An improved time-domain traveling-wave model for vertical-cavity surface-emitting lasers," *IEEE Journal of Quantum Electronics*, Vol. 34, No. 10, 1938–1948, 1998.
27. Xu, T., M. Rossetti, P. Bardella, and I. Montrosset, "Simulation and analysis of dynamic regimes involving ground and excited state transitions in quantum dot passively mode-locked lasers," *IEEE Journal of Quantum Electronics*, Vol. 48, No. 9, 1193–1202, 2012.
28. Berg, T. W. and J. Mørk, "Quantum dot amplifiers with high output power and low noise," *Applied Physics Letters*, Vol. 82, No. 18, 3083–3085, 2003.
29. Zhao, Y.-G. and J. Mcinerney, "Transient temperature response of vertical-cavity surface-emitting semiconductor lasers," *IEEE Journal of Quantum Electronics*, Vol. 31, No. 9, 1668–1673, 1995.
30. Li, W., X. Li, and W.-P. Huang, "A traveling-wave model of laser diodes with consideration for thermal effects," *Optical and Quantum Electronics*, Vol. 36, No. 8, 709–724, 2004.
31. Nakwaski, W. and M. Osinski, "Thermal resistance of top-surface-emitting vertical-cavity semiconductor lasers and monolithic two-dimensional arrays," *Electronics Letters*, Vol. 28, No. 6, 572–574, 1992.